Electrostatic Doping Assisted Push-Pull Mach Zehnder Modulator for Optical Interconnects

Subhradeep Pal[(1)], Soumi Saha[(2)], and Sumanta Gupta[(3)]

(1) School of Electronics Engineering, KIIT, Bhubaneswar, Odisha-751024, India.
(2) Department of Electronics & Communication Engineering, UEM, Kolkata, West Bengal-700160, India.
(3) Department of Electrical Engineering, IIT Patna, Patna, Bihar-801106, India.

Abstract

In this paper, we propose and analyse the performance of an electrostatic doping assisted optical phase shifter loaded push-pull Mach Zehnder modulator (MZM) suitable for short reach optical interconnects. The proposed modulator can be fabricated on standard silicon-on-insulator (SOI) platform and is free from the requirement of highly doped optical waveguide. Theoretical analysis as well as simulation for the performance estimation for the proposed modulator have been presented in this paper. Simulation results indicate that the proposed MZM can support upto 35.2 Gb/s data rate with 4.7 dB of dynamic extinction ratio (ER) and introduces only 5.1 dB of insertion loss (IL). Results also indicates the proposed modulator supports hard decision (HD) FEC BER of 3.8×10^{-3} at 25 Gb/s data rate over a 5 km of standard single mode fiber (SSMF) enabling it suitable for intra-data center optical interconnects.

1 Introduction

Energy efficient high bandwidth integrated optical interconnects have become the potential solution for improvement in overall productivity and efficiency of modern data centers, where the communication traffic has increased exponentially in the past few years [1, 2]. Silicon photonics (SiP) owing to its low cost, and CMOS compatibility is the most accepted technology for the optical interconnects [1, 3]. In these SiP interconnects, integrated silicon modulators play an important role in converting electrical signal into optical signal. Short reach interconnects, which utilizes intensity modulation employs either Mach-Zhender modulator (MZM), or electro-absorption modulator (EAM), or microring modulator (MRM) [3, 4]. Among these modulators, MZM suffers from large device footprint and high power consumption [4], while the performance of MRM largely depends on operating wavelength and temperature [5]. On the other hand, EAM suffers from large device footprint as electro-absorption is very weak in Si. A highly compact and energy efficient optical phase shifter (PS) may be a potential solution to tackle the large footprint problem of the SiP modulators. In general, integrated optical PS utilizes free carrier plasma dispersion effect to achieve a refractive index perturbation in the waveguide, which can be embedded in an interferometric structure to achieve optical intensity modulation. To reduce the overall footprint of the PS, light matter interaction in the waveguide should be improved by increasing the doping concentration in the PS.

Now at increased doping concentration, the performance of the optical PS and thus the SiP modulator gets affected due to random dopant fluctuations (RDF), undesired dopant activation, variation in doping concentration along the length of the PS [6]. To get rid of these problems, recently we have proposed an electrostatic doping (ED) assisted optical PS and we have utilized the ED-assisted PS to propose MZM [5], MRM [7, 8], and EAM [9]. Such ED-assisted PS (utilizes both work-function and bias voltage induced doping) does not contain any chemically doped PN or PIN junction, but still it can be operated in both carrier inversion or accumulation mode. Hence, realization of a push-pull modulator with help of such optical PS is also feasible. In this paper, we propose and analyse the performance of an ED-assisted PS loaded push-pull MZM intended for short reach optical interconnects. In general, the push-pull MZM finds wide applications in analog-optical links [11], mm-wave signal generation [12], and in comb frequency generation [13]. The outline of the paper is as follows. In section 2, we describe the modulator structure, and present an analytical model of the same. Section 3, comprises of simulation methodology, simulation setup and results. In section 4, conclusions are drawn.

2 ED Assisted Push-Pull MZM

2.1 Device Description

Fig. 1 depicts the schematic of the proposed ED assisted push-pull MZM, which contains two ED-assisted PS in the both the arms. The two PS are connected by an integrated power splitter having power splitting ratio $\gamma_1/(1-\gamma_1)$ at the input, and by an integrated power combiner having power combining ratio $\gamma_2/(1-\gamma_2)$ at the output. The length of the both PS is assumed to be 'L' (μm). Fig. 1(b) illustrates the cross-sectional view of the ED-assisted PS. The PS comprises of a 600 nm wide rib waveguide. The device layer is a P-type semiconductor with a doping concentration of $N_A = 10^{17}$ per cc. As depicted in Fig. 1(b), there are five electrodes (three anodes and two controlling elec-
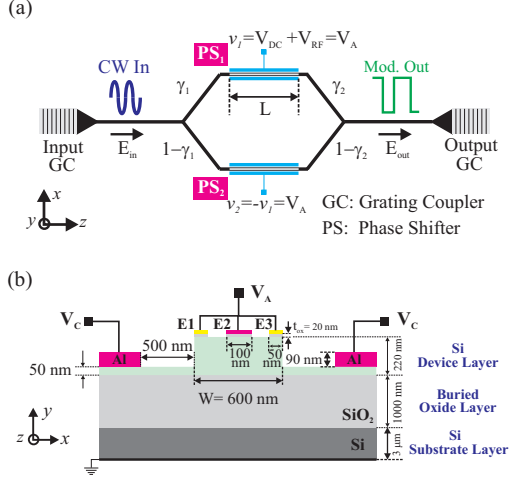
Figure 1. Schematic of proposed ED-assisted MZM: (a) longitudinal view; (b) cross-sectional view of the ED-assisted PS.

Figure 2. Change in carrier concentrations across the rib waveguide at three different anode voltages: (a) 0 V, (b) -5 V and, (c) +5 V.

trodes) present in an ED assisted PS. Among these three anodes, two 50 nm wide electrodes (E1 and E3) are placed on the top at the edges of the waveguide, while a 100 nm wide electrode (E2) is placed centrally on the top of the rib waveguide. A 20 nm thin layer of SiO_2 between the anodes and the top of the rib waveguide is present to prohibit the flow of tunnelling current even at high bias voltages. The optimization of W and t_{ox} are well discussed in [5]. All the three anodes are electrically connected, and these form three different MIS structures on the rib waveguide. There are two aluminum based controlling electrodes present on the clearance region of the rib waveguide forming MS junctions. Both controlling electrodes are 24 nm wide and 90 nm high. Detailed optimization study of the electrode dimensions and spacing between the electrodes is well addressed in [8] and hence skipped here. The controlling electrodes being 500 nm away from the side walls of the rib, do not contribute significantly to the overall modal loss coefficient of the rib. The device layer apart from the rib region is etched down to 50 nm to make the structure compatible with standard input-output grating couplers. The top of the device layer is assumed to be covered with SiO_2. Electrical data is applied on both of the PS after a DC shift (V_{DC}) as shown in Fig. 1(a). In push-pull configuration the two voltages on the two PSs are made complimentary in nature. The operating principle of the ED-assisted PS is explained in [5, 9] and thus not included here.

2.2 Analytical Model

Referring back to Fig. 1(a), the output electric field of the modulated signal (E_{out}) can be expressed as,

$$E_{out} = \left[\sqrt{\gamma_1 \gamma_2} e^{-j\Delta\phi(v_1)} e^{-\Delta\alpha(v_1)L} \right] e^{-j\phi_0} e^{-\alpha_0 L} E_{in}$$
$$+ \left[\sqrt{(1-\gamma_1)(1-\gamma_2)} e^{-j\Delta\phi(v_2)} e^{-\Delta\alpha(v_2)L} \right] e^{-j\phi_0} e^{-\alpha_0 L} E_{in}$$
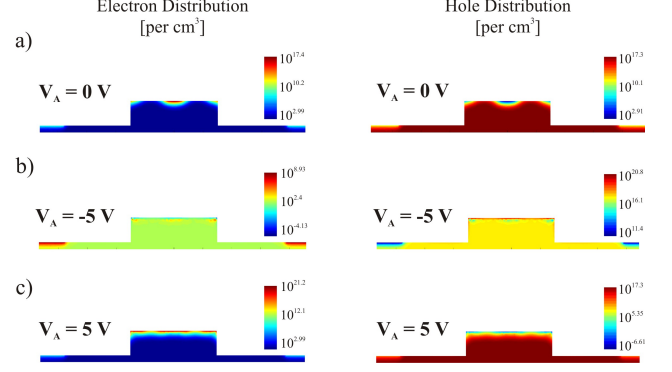$$\tag{1}$$

where $\Delta\phi(v) = 2\pi\Delta n(v)L\lambda^{-1}$, and $\Delta\alpha(v)$ represents the voltage dependent phase and loss coefficient introduced by the PS. ϕ_0 and α_0 are the phase and loss of the PS at zero voltage. Assuming $\gamma_1 = \gamma_2 = \gamma = 0.5$, eqn. (1), can be rewritten as,

$$E_{out} = 0.5 e^{-(\alpha_0 L + j\phi_0)} \left[e^{-j\Delta\phi(v_1)} e^{-\Delta\alpha(v_1)L} + e^{-j\Delta\phi(v_2)} e^{-\alpha(v_2)L} \right] E_{in}$$
$$\tag{2}$$

Optimizing γ_1 in eqn. (1), higher dynamic extinction ratio (ER) of the proposed modulator can be achieved.

3 Simulation Results

3.1 Simulation Methodology and Test Setup

For estimating the performance of the proposed device, we have used the similar design parameters of the noble electrode based MZM as discussed in [5]. The carrier information inside the rib waveguide is numerically calculated at different anode voltages (V_A) using a commercial-grade device simulator, which self-consistently solves the Poisson and drift-diffusion equations (Lumerical Device CT) [14]. Fig. 2 depicts the carrier concentration for different values of V_A. Using the carrier information, change in refractive index (Δn) and change in loss coefficient ($\Delta\alpha$) at 1550 nm can be obtained from the modified Soref's relations [15] as,

$$\Delta n = -5.4 \times 10^{-22} \Delta N_e^{1.011} - 1.53 \times 10^{-18} \Delta N_h^{0.838} \tag{3}$$
$$\Delta \alpha = 8.88 \times 10^{-21} \Delta N_e^{1.167} + 5.84 \times 10^{-20} \Delta N_h^{1.109} \tag{4}$$

where ΔN_e and ΔN_h are change in the electron and hole concentration per cc, respectively. For the determination of modal effective refractive index and loss coefficient at different V_A, we have used a commercial grade simulator, Lumerical Mode Solutions [16]. Using the estimated value of Δn, $\Delta\alpha$, and the system depicted in Fig. 3 we have estimated the performance of the proposed modulator using Lumerical Interconnect [17].
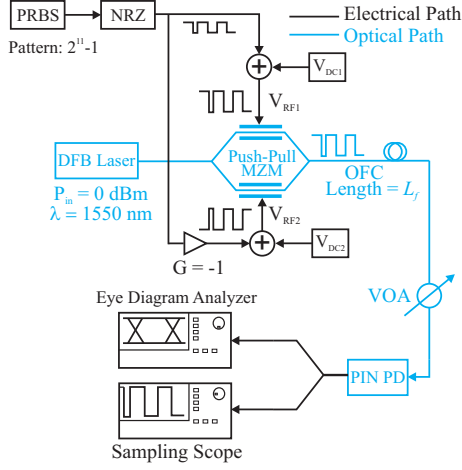
Figure 3. Simulation test setup utilized to estimate the transient and BER performance of the proposed modulator.
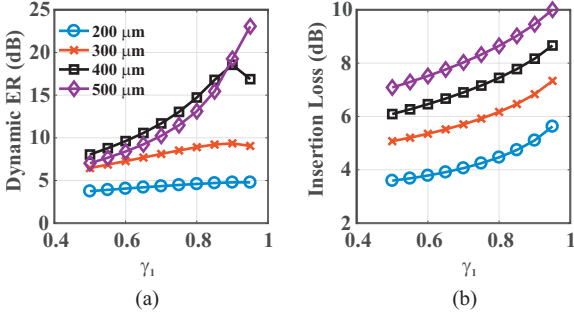

Figure 4. Performance of the proposed modulator in terms of (a) dynamic ER, (b) IL, with varying L and γ_1. For simulation, we have utilized a 25 Gb/s, $2^{11} - 1$ PRBS signal.

3.2 Steady State Performance

At first, we have estimated the value of $V_\pi L_\pi$ for PS_1 and PS_2. For $\lambda = 1.55$ μm, the estimated value of $V_\pi L_\pi$ for PS_1 and PS_2 are 0.36 V.cm and 0.74 V.cm, respectively. PS_1 exhibits better performance compared to PS_2 as ΔN_h is high in carrier inversion mode. For the optimization of L and γ_1, we have varied L from 200 μm to 500 μm in a step of 100 μm, while γ_1 is varied from 0.5 to 0.95 in a step of 0.05. In the simulation, we have also assumed an excess loss of 0.36 dB for the both power coupler and splitter. Since the two PS are operating in two different conditions, losses in the both arms of the MZM will be different. For $L = 200$ μm, PS_1 and PS_2 introduces 3.34 dB, and 0.85 dB of IL, respectively. Hence, an asymmetric power splitter at the input section will enhance the dynamic ER of the modulator. Simulation results depicted in Fig. 4 supports the same. The estimated dynamic ERs of the 400 μm long MZM for $\gamma_1 = 0.5$, and 0.9, are approximately 8 dB and 18.6 dB, respectively. For $\gamma_1 = 0.9$, the proposed modulator with L = 200 μm, 300 μm, and 500 μm offers approximately 4.8 dB, 9.3 dB, and 19.2 dB, respectively. Evidently, the dynamic ER increases with the length of PS (refer to Fig. 4(a)). However, this improvement comes in the cost of IL and 3-dB electro-optic (EO) bandwidth [5].
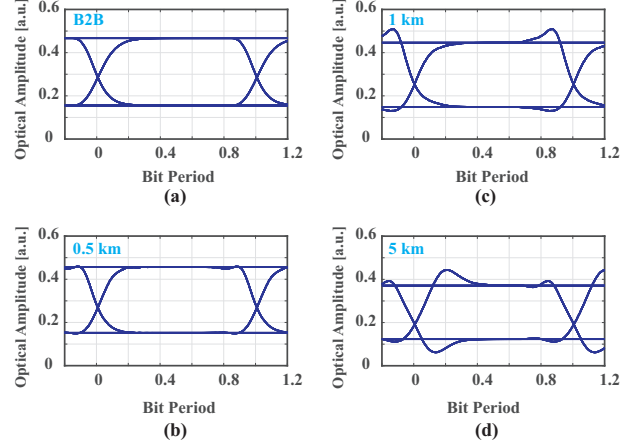

Figure 5. Simulated optical eye diagram of the modulated optical signal at: (a) B2B, after (b) 0.5 km, (c) 1 km, and (d) 5 km. Input data rate is selected at 10 Gb/s.

3.3 Transient Performance

To study the transient performance of the modulator, we have provided a $2^{11} - 1$ PRBS signal of amplitude 5 V with a 3 V DC offset at 10 Gb/s to drive the modulator with $L = 200$ μm and $\gamma_1 = 0.9$. The corresponding optical eye diagram of the modulated signal at back-to-back condition (B2B), and after $L_f = 0.5$, 1, and 5 km are shown in Fig. 5. The estimated dynamic ER is found to be approximately 4.8 dB. At 25 Gb/s, the modulator with L = 200 μm and $\gamma_1 = 0.5$ offers approximately 3.8 dB of dynamic ER and 3.6 dB of IL (refer Fig. 4) which is higher even for the specified ER of 3.5 dB for short reach interconnects [18]. Using the method described in [5], we have found that the proposed modulator of $L = 200$ μm, and 400 μm will offer approximately 28 GHz and 22.7 GHz of 3-dB EO bandwidth, respectively. For such modulators, the estimated maximum operating speed (f_{max}) are 35.2 GHz and 30.3 GHz, respectively. As discussed in [5], for large values of L, the modulator suffers from the high capacitances originating at the three MIS junctions. Thus, for high speed operation it is absolutely essential to choose the value of L as low as possible.

For the estimation of BER performance, we have selected the modulator with $L = 400$ μm. We have driven the modulator at 25 Gb/s data rate with a $2^{11} - 1$ PRBS signal. For the test link, we have varied L_f from 0.5 km to 5 km and at the receiver end we have used a PIN photodetector (PD) (refer to Fig. 3). For the PIN diode, we have considered a thermal noise of -410 dBm/Hz and responsivity of 0.85 A/W. Also, 5 nA of dark current for the PIN PD is considered. The simulated BER performance for the proposed modulator at 25 Gb/s data rate is shown in Fig. 6. From the results, we can conclude that the proposed modulator can achieve the HD-FEC BER limit easily even for a 5 km long SSMF link. The estimated power penalty of the SSMF link at 0.5, 1, and 5 km for pre-FEC BER are 2.5 dB, 5 dB, and 13 dB, respectively. However, it is
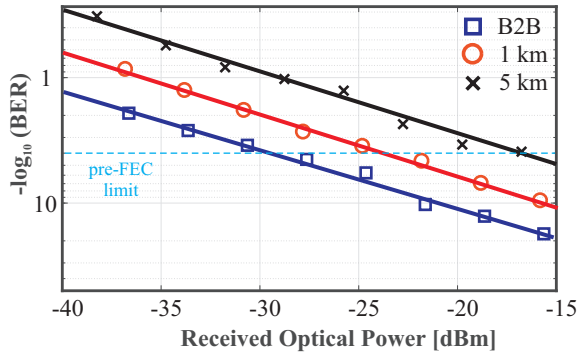
Figure 6. Simulated BER performance of the proposed modulator at 25 Gb/s.

Table 1. Performance comparison of the proposed MZM.

Reference	Year	Material	L [mm]	ER [dB]	IL [dB]	f_{max} [GHz]	$V_\pi L_\pi$ [V.cm]
[10]	2019	Si	3	3.6	9.1	32	0.55
[11]	2019	Si$-$LiNbO$_3$	3	5.0	2.5	112	2.20
[19]	2019	AlGaAs	10	3.0	7.5	-	1.00
This work	2020	Si	0.2	4.7	5.1	30.3	0.36-0.74

worthy to note that the power penalty of the link may be reduced further by using DSP based dispersion mitigation algorithms at the receiver end. Also, we have compared the performance of the proposed MZM with some recently reported push-pull MZMs in Table-1. From the comparison, we can conclude that the proposed modulator offers significant improvement in terms of length. Although the proposed modulator offers a similar dynamic ER but it has a limited maximum operating speed.

4 Conclusions

An ED-assisted optical PS loaded push-pull MZM is proposed and its performance is analyzed in this paper. An analytical model of the proposed MZM is also presented here. Simulation results indicate that, a 200 μm long push-pull MZM offers almost 4.7 dB of dynamic ER at 10 Gb/s data rate with 5.1 dB of IL. We have also optimized the value of γ_1 and L as a function of the dynamic ER and IL. From the results, we can also conclude that asymmetric power splitting in the input section of the modulator will increase the dynamic ER of such modulators. For 200 μm long modulator, the estimated value of f_{max} and 3-dB EO BW are 35.2 GHz, and 28 GHz, respectively. BER performance analysis confirms that, the proposed modulator based SSMF link can achieve HD-FEC BER limit at 25 Gb/s data rate.

References

[1] M. R. Tan, P. Rosenberg, W. V. Sorin, B. Wang, S. Mathai, G. Panotopoulos, and G. Rankin, "Universal photonic interconnect for data centers," *Journal of Lightwave Technology*, vol. 36, no. 2, pp. 175–180, 2018.

[2] S. Rumley, M. Bahadori, R. Polster, S. D. Hammond, D. M. Calhoun, K. Wen, A. Rodrigues, and K. Bergman, "Optical interconnects for extreme scale computing systems," *Parallel Computing*, vol. 64, pp. 65–80, 2017.

[3] J. Witzens, "High-speed silicon photonics modulators," *Proceedings of the IEEE*, vol. 106, no. 12, pp. 2158–2182, Dec 2018.

[4] D. Marris-Morini, L. Vivien, G. Rasigade, J.-M. Fedeli, E. Cassan, X. Le Roux, P. Crozat, S. Maine, A. Lupu, P. Lyan *et al.*, "Recent progress in high-speed silicon-based optical modulators," *Proceedings of the IEEE*, vol. 97, no. 7, pp. 1199–1215, 2009.

[5] S. Pal and S. Gupta, "Junction-less optical phase shifter loaded silicon mach-zehnder modulator," *Optics Communications*, vol. 437, pp. 110 – 120, 2019.

[6] C. Shin *et al.*, *Variation-aware advanced CMOS devices and SRAM*. Springer, 2016, vol. 56.

[7] S. Pal and S. Gupta, "Performance analysis of an electrostatic doping assisted silicon microring modulator," *Optics Communications*, vol. 430, pp. 131–138, 2019.

[8] ——, "Nonlinear performance and small signal model of junction-less microring modulator," *Optics Communications*, vol. 459, p. 124984, 2020.

[9] S. Pal, P. K. Tiwari, and S. Gupta, "A proposal for an electrostatic doping-assisted electroabsorption modulator for intrachip communication," *IEEE Transactions on Electron Devices*, vol. 66, no. 5, pp. 2269–2275, May 2019.

[10] G. Zhou, L. Zhou, Y. Guo, L. Liu, L. Lu, and J. Chen, "High-efficiency silicon mach-zehnder modulator with u-shaped pn junctions," in *CLEO: Applications and Technology*. Optical Society of America, 2019, pp. JTh2A–42.

[11] M. He, M. Xu, Y. Ren, J. Jian, Z. Ruan, Y. Xu, S. Gao, S. Sun, X. Wen, L. Zhou *et al.*, "High-performance hybrid silicon and lithium niobate mach–zehnder modulators for 100 gbit s- 1 and beyond," *Nature Photonics*, vol. 13, no. 5, pp. 359–364, 2019.

[12] X. Pan, X. Liu, H. Zhang, C. Wang, X. Wang, Y. Zhang, and D. Ran, "Photonic vector mm-wave signal generation by optical dual-ssb modulation and a single push-pull mzm," *Optics letters*, vol. 44, no. 14, pp. 3570–3573, 2019.

[13] Z. Wang, M. Ma, H. Sun, M. Khalil, R. Adams, K. Yim, X. Jin, and L. R. Chen, "Optical frequency comb generation using cmos compatible cascaded mach–zehnder modulators," *IEEE Journal of Quantum Electronics*, vol. 55, no. 6, pp. 1–6, 2019.

[14] Lumerical device r2018a r3. [Online]. Available: http://www.lumerical.com/tcad-products/device/

[15] M. Nedeljkovic, R. Soref, and G. Z. Mashanovich, "Free-carrier electrorefraction and electroabsorption modulation predictions for silicon over the 1–14 μm infrared wavelength range," *IEEE Photonics Journal*, vol. 3, no. 6, pp. 1171–1180, Dec 2011.

[16] Lumerical mode solutions r2018a r3. [Online]. Available: http://www.lumerical.com/tcad-products/mode/

[17] Lumerical interconnect r2018a r3. [Online]. Available: http://www.lumerical.com/tcad-products/interconnect/

[18] C. Gunn, "Cmos photonics for high-speed interconnects," *IEEE Micro*, vol. 26, no. 2, pp. 58–66, 2006.

[19] P. Bhasker, J. Norman, J. E. Bowers, and N. Dagli, "Low voltage, high optical power handling capable, bulk compound semiconductor electro-optic modulators at 1550 nm," *Journal of Lightwave Technology*, 2020.